CHEMISTRY OF MATERIALS
Article

Chem. Mater. **2009,** *21,* 5527–5538 5527
DOI:10.1021/cm902535m

Synthesis and Structural Characterization of $La_{1-x}A_xMnO_{2.5}$ (A = Ba, Sr, Ca) Phases: Mapping the Variants of the Brownmillerite Structure

Thomas G. Parsons,[†] Hans D'Hondt,[‡] Joke Hadermann,[‡] and Michael A. Hayward*,[†]

[†]*Department of Chemistry, Inorganic Chemistry Laboratory, University of Oxford, South Parks Road, Oxford OX1 3QR, United Kingdom, and* [‡]*EMAT, University of Antwerp, Groenenborgerlaan 171, B-2020 Antwerp, Belgium*

Received August 18, 2009. Revised Manuscript Received October 8, 2009

Analysis of the structural parameters of phases that adopt brownmillerite-type structures suggests the distribution of the different complex ordering schemes adopted within this structure type can be rationalized by considering both the size of the separation between the tetrahedral layers and the tetrahedral chain distortion angle. A systematic study using structural data obtained from $La_{1-x}A_xMnO_{2,5}$ (A = Ba, Sr, Ca,) phases, prepared by the topotactic reduction of the analogous $La_{1-x}A_xMnO_3$ perovskite phases, was performed to investigate this relationship. By manipulating the A-cation composition, both the tetrahedral layer separation and tetrahedral chain distortion angle in the $La_{1-x}A_xMnO_{2,5}$ phases were controlled and from the data obtained a "structure map" of the different brownmillerite variants was plotted as a function of these structural parameters. This map has been extended to include a wide range of reported brownmillerite phases showing the structural ideas presented are widely applicable. The complete structural characterization of $La_{1-x}A_xMnO_{2,5}$ $0.1 \le x \le 0.33$, A = Ba; $0.15 \le x \le 0.5$ A = Sr, and $0.22 \le x \le 0.5$ A = Ca is described and includes compositions which exhibit complex intralayer ordered structures and Mn^{2+}/Mn^{3+} charge ordering.

Introduction

Transition metal oxides have been of enduring interest to scientists in a wide range of fields because of the diverse physical properties they exhibit. These include superconductivity, magnetoresistance, and wealth of cooperative magnetic and transport behaviors. The introduction of large numbers of anion vacancies into transition metal oxides allows the tuning of these physical properties by altering the oxidation state and local coordination of transition metal centers. In addition, the presence of a large number of vacant anion sites can induce good ionic conductivity, giving these phases applications as fuel cell electrodes and membranes. The efficiency of ionic transport in anion deficient systems has been shown to be strongly influenced by the degree of order or disorder in the anion vacancy lattice. The potential future importance of these applications strongly motivates the study of anion deficient materials to investigate factors that direct this ordering behavior so that better property optimizations can be achieved.[1,2]

The brownmillerite structure is one of the most common anion vacancy ordered structures.[3] It can be viewed as an anion-deficient variant of the ABO_3 cubic perovskite structure in which half the anions have been removed from alternate BO_2 layers. This gives the stacking sequence AO-BO_2-AO-BO-AO- with alternating layers of apex-linked BO_6 octahedra and BO_4 tetrahedra (Figure 1). The anion vacancies are arranged within the BO layers in an ordered manner to yield chains of vacancies parallel to the [110] direction of the simple cubic perovskite lattice. The resulting layers consist of chains of apex-linked BO_4 tetrahedra which also run along the [110] direction of the simple cubic perovskite sublattice. The structure is complicated by the possibility that the chains of tetrahedra can undergo a cooperative twist, which can occur in either a clockwise or anti-clockwise sense, to yield "left"- or "right"-handed chains (Figure 2)—the two being related by symmetry.

The three-dimensional arrangement of the different twist directions within the structure leads to a number of distinct structural configurations (Figure 1). The simplest ordered arrangement in which all the tetrahedral chains are twisted in the same manner is described in space group *I2mb*. In contrast the configuration with Pnma symmetry has all the tetrahedral chains in a particular layer twisted in the same manner, but the twist direction inverts between adjacent layers (interlayer order). There are also configurations that adopt an alternating arrangement of left and right handed chains within the tetrahedral layers (intralayer order). These ordered layers can be stacked in one of two ways: either with a

*Corresponding author. E-mail: michael.hayward@chem.ox.ac.uk. Tel.: +44 1865 272623. Fax: +44 1865 272690.

(1) Mohn, C. E.; S., S.; Norberg, S. T.; Hull, S. *Phys. Rev. Lett.* **2009**, *102*, 155502.
(2) Stolen, S.; Mohn, C. E.; Ravindran, P.; Allan, N. L. *J. Phys. Chem. B* **2005**, *109*, 12362–12365.
(3) Anderson, M. T.; Vaughey, J. T.; Poeppelmeier, K. R. *Chem. Mater.* **1993**, *5*, 151–165.

Published on Web 10/29/2009

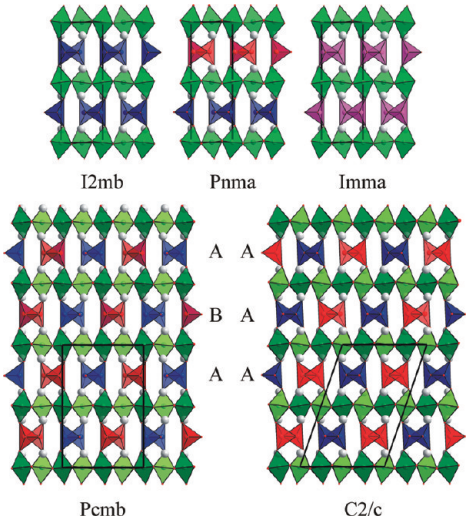

Figure 1. Five common variants of the brownmillerite structure.

stacking vector of 1/2[111] (type A stacking) which displaces like-twisted chains in the 'new' layer to the right of those in the "old" layer, or with a stacking vector of 1/2[11$\bar{1}$]) (type B stacking) which displaces like-twisted chains in the "new" layer to the left of those in the "old" layer. A large number of complex stacking sequences can be generated by combining these two stacking types;[4] however, the simplest are the AAAA sequence that generates a bulk structure that is described in the space group $C2/c$ and an ABAB sequence that generates a bulk structure described in the space group *Pcmb* as shown in Figure 1.[5] The former model has previously been described in the space group $P2_1/c$,[6] but as explained later this can be simplified into a higher symmetry $C2/c$ description. More complex stacking sequences can result in structures with incommensurate tetrahedral chain ordering,[4] or brownmillerite structures in which there is no long range ordering of the twisted tetrahedral chains. These disordered structures are described in the space group Imma (Figure 1).

There has been much debate as to the driving force for the adoption of these different ordering schemes. Abakumov et al. proposed a model based on the stabilization of the dipole moments which are created along the tetrahedral chains when they are twisted (Figure 2).[7] This was built on by Hadermann et al., who added to this the influence of the separation between tetrahedral layers in combination with the tetrahedral chain distortion.[8] However, a dearth of well-characterized phases that adopt complex brownmillerite

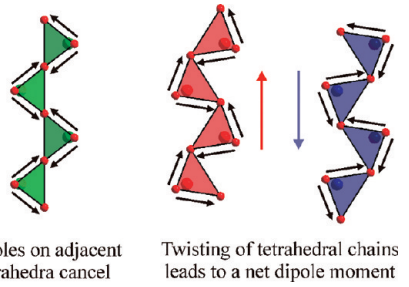

Figure 2. Twisting distortion of tetrahedral chains leads to a net dipole moment.

structures, particularly those that adopt the $C2/c$ and *Pcmb* structural variants, has hampered the expansion of these ideas. Here, we present detailed structural data from a large number of related brownmillerite phases that allow these ideas to be tested rigorously.

The observation of large magnetoresistive effects in the brownmillerite phase $SrCaMnGaO_{5.04}$[9] directed interest toward phases of this structure type. Recently we have demonstrated that mixed valent Mn(II)/Mn(III) phases can be prepared by the topotactic reduction of Mn(III)/Mn(IV) perovskites using sodium hydride (NaH) as a solid-state reducing agent.[10] The phases thus formed adopt brownmillerite-like anion deficient structures and exhibit charge ordering between Mn(II) and Mn(III) centers for suitable compositions.[6] In order to investigate this behavior, we were motivated to prepare a range of related phases of composition $La_{1-x}A_xMnO_{2.5}$ (A = Ba, Sr, Ca) which constitute a series of mixed-valence Mn(II)/Mn(III) oxides analogous to the widely studied Mn(III)/Mn(IV) perovskite phases.

Experimental Section

Preparation of $La_{1-x}A_xMnO_3$ Phases. Samples of $La_{1-x}A_xMnO_3$ were prepared via a citrate gel method. The appropriate stoichiometric ratios of La_2O_3 (99.999 %, dried at 900 °C), $BaCO_3$ (99.997 %), $SrCO_3$ (99.994 %), $CaCO_3$ (99.999 %), and MnO_2 (99.999 %) were dissolved in a minimum quantity of 6 M nitric acid. Two molar equivalents of citric acid and 5 mL of analar ethylene glycol were added and the solutions heated with constant stirring. The gels thus formed were subsequently ground into a fine powder, placed in an alumina crucible, and heated at 1 °C min^{-1} to 900 °C in air. The powders were then ground again and pressed into 13 mm pellets under a force of 5 tonnes. The $La_{1-x}Sr_xMnO_3$ and $La_{1-x}Ca_xMnO_3$ samples were fired at 1325 and 1350 °C, respectively, in air for two periods of 2 days.[11−13] A final heating was performed at 1350 °C under flowing argon to ensure that there were no manganese vacancies present in the materials due to oxidation.[14] The

(4) D'Hondt, H.; Abakumov, A. M.; Hadermann, J.; Kalyuzhnaya, A. S.; Rozova, M. G.; Antipov, E. V.; Van Tendeloo, G. *Chem. Mater.* **2008**, *20*, 7188–7194.
(5) Abakumov, A. M.; Alekseeva, A. M.; Rozova, M. G.; Antipov, E. V.; Lebedev, O. I.; Van Tendeloo, G. *J. Solid State Chem.* **2003**, *174*, 319–328.
(6) Casey, P. S.; Barker, D.; Hayward, M. A. *J. Solid State Chem.* **2006**, *179*, 1375–1382.
(7) Abakumov, A. M.; Kalyuzhnaya, A. S.; Rozova, M. G.; Antipov, E. V.; Hadermann, J.; Van Tendeloo, G. *Solid State Sci.* **2005**, *7*, 801–811.
(8) Hadermann, J.; Abakumov, A. M.; D'Hondt, H.; Kalyuzhnaya, A. S.; Rozova, M. G.; Markina, M. M.; Mikheev, M. G.; Tristan, N.; Klingeler, R.; Buchner, B.; Antipov, E. V. *J. Mater. Chem.* **2007**, *17*, 692–698.
(9) Battle, P. D.; Bell, A. M. T.; Blundell, S. J.; Coldea, A. I.; Gallon, D. J.; Pratt, F. L.; Rosseinsky, M. J.; Steer, C. A. *J. Solid State Chem.* **2002**, *167*, 188–195.
(10) Hayward, M. A.; Green, M. A.; Rosseinsky, M. J.; Sloan, J. *J. Am. Chem. Soc.* **1999**, *121*, 8843–8854.
(11) Chmaissem, O.; Dabrowski, D.; Kolesnik, S.; Mais, J.; Jorgensen, J. D.; Short, S. *Phys. Rev. B* **2003**, *67*, 94431.
(12) Dabrowski, B.; Dybzinski, R.; Bukowski, R.; Chmaissem, O.; Jorgensen, J. D. *J. Solid State Chem.* **1999**, *146*, 448–457.
(13) Rormark, L.; Wiik, K.; Stolen, S.; Grande, T. *J. Mater. Chem.* **2002**, *12*, 1058–1067.
(14) Krogh Andersen, I. G.; Krogh Andersen, E.; Norby, P.; Skou, E. *J. Solid State Chem.* **1994**, *113*, 320–326.

$La_{1-x}Ba_xMnO_3$ samples were heated under flowing argon at 1500 °C for two periods of 24 h. The reducing conditions provided by the argon promote the formation of cubic perovskite phases over hexagonal perovskite phases.[15,16] After being cooled, the pellets were reground and the resulting powders heated in an alumina boat at 400 °C under flowing oxygen for 12 hours to achieve full oxygen stoichiometry. X-ray powder diffraction patterns collected from all $La_{1-x}A_xMnO_3$ phases (A = Ba, Sr, Ca) confirmed that pure single-phase samples had been formed with lattice parameters in good agreement with published values.[11−16]

Reduction of $La_{1-x}A_xMnO_3$ Phases. The reduction of $La_{1-x}A_xMnO_3$ phases was performed using sodium hydride (Aldrich > 95%) as has been described previously.[6] $La_{1-x}A_xMnO_3$ samples were ground thoroughly in an argon-filled glove box (O_2 and H_2O < 1ppm) with a double-stoichiometric quantity of NaH. The resulting mixtures were then sealed under vacuum in Pyrex tubes and heated for 1 day at 200 °C and then at 210 °C for a further day. The samples were reground and then heated for 2 days at 215 °C and, after a further grinding, at 220 °C for 2 more days. Samples were then washed under nitrogen with 4 × 100 mL of methanol to remove sodium containing phases (NaOH and NaH) before being dried under a vacuum.

Characterization Methods. X-ray powder diffraction data were collected using a PANalytical X'Pert diffractometer incorporating an X'celerator position sensitive detector (monochromatic Cu $K_{\alpha 1}$ radiation). Data were collected from air-sensitive samples under an inert atmosphere using a homemade gas-tight sample holder. Neutron powder diffraction data were collected from selected samples contained in vanadium cans sealed with an indium washer under an argon atmosphere. Data were collected using the D2b diffractometer (λ = 1.59 Å) at the ILL neutron source, Grenoble. In addition neutron diffraction data were collected from a sample of $La_{0.8}Sr_{0.2}MnO_{2.5}$ using the POLARIS diffractometer at the ISIS neutron source, UK. Rietveld profile refinement was performed using the GSAS suite of programs.[17] The samples for electron microscopy investigation were prepared by crushing the powder sample in ethanol and depositing it on a holey carbon grid. Electron diffraction (ED) studies were performed using a Philips CM20 microscope. Thermogravimetric reoxidation measurements were preformed by heating powdered samples under flowing oxygen using a Netzsch STA 409PC balance.

Results

Extent of the Brownmillerite Phase Range. X-ray powder diffraction data collected from reduced $La_{1-x}A_xMnO_{3-y}$ (A = Ba, Sr, Ca) phases revealed brownmillerite type structures were adopted for a limited range of La^{3+}/A^{2+} cation ratios as shown in Figure 3. For the barium containing phases this range was observed to be $0.1 \le x \le 0.33$. Phases with larger values of x adopted structures with cubic symmetry suggestive of disordered anion vacancy distributions; phases with smaller values of x appear to adopt much more complex anion vacancy

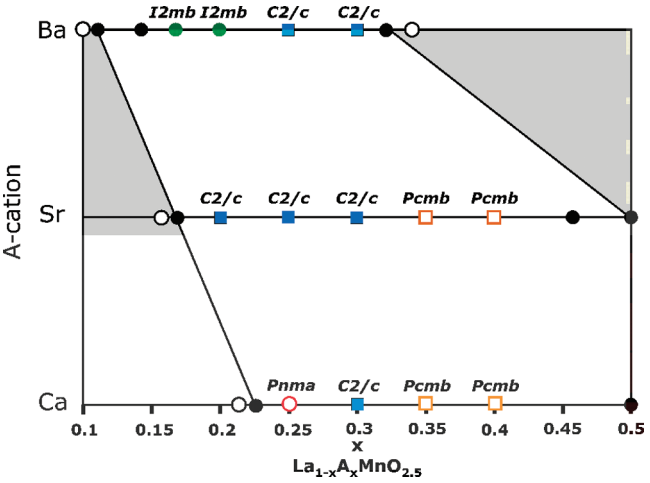

Figure 3. The compositional extent of brownmillerite phases in $La_{1-x}A_xMnO_{2.5}$ (A = Ba, Sr, Ca) series. Closed black symbols represent brownmillerite compositions, open black symbols represent non-brownmillerite compositions. Phases studied by neutron and electron diffraction are marked with the appropriate space group. $La_{0.5}Sr_{0.5}MnO_{2.5}$ and $La_{0.5}Ca_{0.5}MnO_{2.5}$[20,21] are included for completeness.

ordering schemes than present in brownmillerite structures and will be described elsewhere. The strontium and calcium containing phases adopt brownmillerite structures in the range $0.15 \le x \le 0.5$ and $0.22 \le x \le 0.5$, respectively. Samples with values of x smaller than these ranges (lanthanum-rich) contain a complex mixture of phases and will not be discussed further here; samples with values of $x > 0.5$ yielded complex layered structures when reduced with sodium hydride, which will be discussed elsewhere. This is in contrast to the series of anion deficient phases of composition $La_{1-x}Sr_xMnO_{3-d}$ ($0.6 < x < 0.9$), prepared by reduction with hydrogen at higher temperatures, which have recently been reported by Suescun et al.[18,19] The anion vacancy distribution in these phases leads to structures with octahedral and 5-coordinate square-based pyramidal coordinations for manganese, rather than brownmillerite type structures. Samples of composition $La_{0.5}Ca_{0.5}MnO_{2.5}$ and $La_{0.5}Sr_{0.5}MnO_{2.5}$ prepared in this study exhibited extensive micro-twining which prevented their detailed structural characterization and so will not be discussed further here. These phases have previously been reported by Gonzalez-Calbet and coworkers.[20,21]

Characterization of $La_{1-x}A_xMnO_{2.5}$ Phases. Thermogravimetric reoxidation measurements performed on the $La_{1-x}A_xMnO_{3-y}$ (A = Ba, Sr, Ca) samples prepared in this study were all consistent with formulations of $La_{1-x}A_xMnO_{2.5}$. Plots of these data are given in the Supporting Information. X-ray powder diffraction data

(15) Dabrowski, B.; Rogacki, K.; Xiong, X.; Klamut, P. W.; Dybzinski, R.; Shaffer, J. *Phys. Rev. B* **1998**, *58*, 2716–2723.
(16) Barnabe, A.; Millange, F.; Maignan, A.; Hervieu, M.; Raveau, B. *Chem. Mater.* **1998**, *10*, 252–259.
(17) Larson, A. C.; Von Dreele, R. B. *General Structure Analysis System*; Los Alamos National Laboratory Report LAUR 86-748; Los Alamos National Laboratory: Los Alamos, NM, 2000.
(18) Suescun, L.; Dabrowski, D.; Remsen, S.; Mais, J. *J. Solid State Chem.* **2009**, *182*, 187–195.
(19) Suescun, L.; Dabrowski, B.; Mais, J.; Remsen, S.; Richardson, J. W.; E.R., M.; Jorgensen, J. D. *Chem. Mater.* **2008**, *20*, 1636–1645.
(20) Gonzalez-Calbet, J. M.; Herrero, E.; Rangavittal, N.; Alonso, J. M.; Martinez, J. L.; Vallet-Regi, M. *J. Solid State Chem.* **1999**, *148*, 158–169.
(21) Cortes-Gil, R.; Ruiz-Gonzalez, M. L.; Alonso, J. M.; Vallet-Regi, M.; Hernando, M.; Gonzalez Calbet, J. M. *Chem−Eur. J.* **2007**, *13*, 4246–4252.

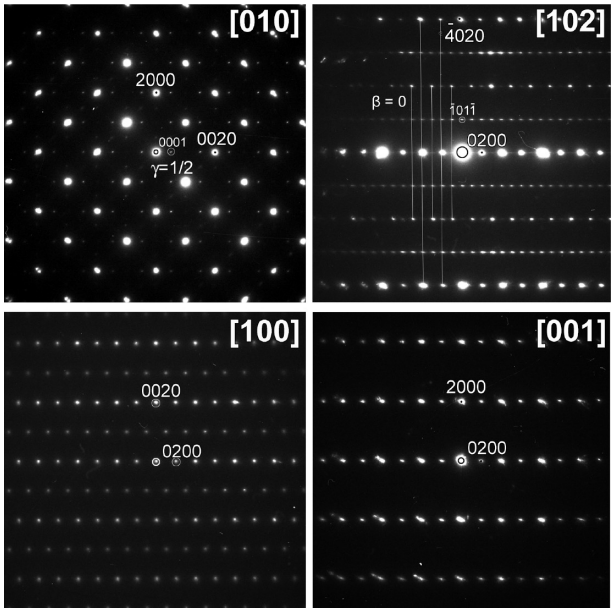

Figure 4. Electron diffraction data collected from $La_{0.65}Sr_{0.35}MnO_{2.5}$. Lines are drawn through several neighboring reflections as a guide to the eye for comparison with Figure 5. The indexation shown is that in the (3+1)D space group $Imma(00\gamma)s00$.

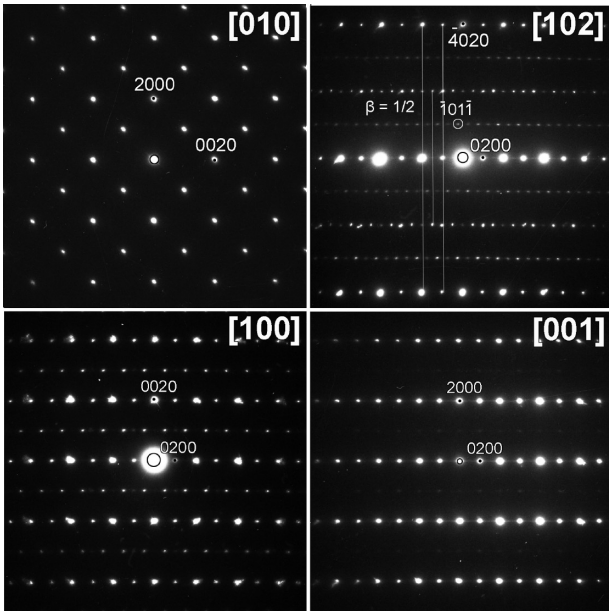

Figure 5. Electron diffraction data collected from $La_{0.7}Sr_{0.3}MnO_{2.5}$. Lines are drawn through several neighboring reflections as a guide to the eye for comparison with figure 4. The indexation shown is that in the (3+1)D space group $I2/m(0\beta\gamma)0s$.

collected from the $La_{1-x}A_xMnO_{2.5}$ samples could be readily indexed on the basis of orthorhombic unit cells, which can be described as a $\sqrt{2}a_p$, $4a_p$, $\sqrt{2}a_p$ transformation of a simple cubic perovskite cell (a_p) consistent with brownmillerite type structures. Because of the low sensitivity of X-ray powder diffraction to the location of oxide ions in the presence of much heavier elements, electron and neutron diffraction were used to fully structurally characterize the reduced materials.

Structural Refinement of $La_{1-x}Sr_xMnO_{2.5}$ (x = 0.4, 0.35, 0.3, 0.25, 0.2). Models corresponding to the five variants of the brownmillerite structure were refined against neutron powder diffraction data collected from $La_{-x}Sr_x$-$MnO_{2.5}$ phases. It can be seen from fitting statistics in Table S1 in the Supporting Information that according to the neutron diffraction data, all the $La_{1-x}Sr_xMnO_{2.5}$ phases adopt either the $C2/c$ ($x = 0.2$, 0.25, 0.3) or $Pcmb$ ($x = 0.35$, 0.4) structure variants, in which the twist direction of the tetrahedral chains alternates within a tetrahedral layer. As described previously, the difference between these two structural descriptions ($C2/c$ and $Pcmb$) is subtle and so in order to unambiguously establish which variant is adopted, electron diffraction data were collected.

A recent structural reinvestigation of $Sr_2Fe_2O_5$[4] has demonstrated that electron diffraction data are particularly sensitive to the tetrahedral chain order in brownmillerite phases, as it leads to a change in crystallographic symmetry. The $Sr_2Fe_2O_5$ study showed that if electron diffraction data were indexed utilizing an incommensurate description with four indices, $hklm$, in which the diffraction vector is $\mathbf{g} = h\boldsymbol{a}^* + k\mathbf{b}^* + l\mathbf{c}^* + m\mathbf{q}$ with either $\mathbf{q} = \beta\mathbf{b}^* + \gamma\mathbf{c}^*$ in (3+1)D space group $I2/m(0\beta\gamma)0s$ or $\mathbf{q} = \gamma\mathbf{c}^*$ in (3+1)D space group $Imma(00\gamma)s00$. The 3D space group for commensurately modulated structures can be deduced for the rational values of β and γ.[4]

Electron diffraction data collected from $La_{0.65}Sr_{0.35}$-$MnO_{2.5}$ could be readily indexed by this method. Figure 4 shows electron diffraction patterns collected from different zones of $La_{0.65}Sr_{0.35}MnO_{2.5}$. Strong satellite peaks along the $\mathbf{c}^*$ direction in the [010] pattern at 1/2(001) indicate $\gamma = 1/2$. Analysis of the [102] zone allows us to deduce $\beta = 0$ (see also Figure 5 in ref 4), and thus the modulation vector $\mathbf{q} = 1/2\mathbf{c}^*$. The reflection conditions that are present correspond to the space group $Imma(00\gamma)s00$ with lattice parameters $\sqrt{2}a_p$, $4a_p$, $\sqrt{2}a_p$. According to Table 2 in ref 4, in 3D one of the space groups $Pcmb$, $Pcma$, or $Pcm2_1$ can be used that allow 3D representations with lattice parameters $\sqrt{2}a_p$, $4a_p$, $2\sqrt{2}a_p$ of the same (3+1)D structure. It should be noted that because the projected structure factors F_R and F_L associated with the "right" and "left" tetrahedral chains are identical along several crystallographic directions, more reflections are extinct than strictly given by the reflection conditions of the particular 3D space groups. The $Pcmb$ space group was chosen because it produces a completely ordered arrangement of the tetrahedral chains. An analogous analysis of the data collected from $La_{0.6}Sr_{0.4}MnO_{2.5}$ indicates this phase also allows the $Pcmb$ type structural model as detailed in the Supporting Information.

The analysis of electron diffraction data collected from $La_{0.7}Sr_{0.3}MnO_{2.5}$ gives a different result. Data collected from the [100], [010], and [001] zones of $La_{0.7}Sr_{0.3}MnO_{2.5}$ exhibit no satellite reflections (Figure 5). Inspection of the [102] zone however revealed a series of satellites which, when indexed with the four incommensurate indices described above, require a value of $\beta = 1/2$ (Figure 5) (see also Figure 5 of ref 4, taking into account the occurrence of twinning). The reflections conditions and modulation vectors correspond to a (3+1) space group

$I2/m(0\beta\gamma)0$s. This will allow the $C2/c$ and Cc variants of the brownmillerite structure according to Table 2 of ref 4. Analogous analysis of the data collected from $La_{0.75}Sr_{0.25}MnO_{2.5}$ and $La_{0.8}Sr_{0.2}MnO_{2.5}$ revealed these phases also allow the $C2/c$ structural variant, consistent with previous reports.[6] Thus it can be seen that electron diffraction data gives unambiguous information from which the correct space groups can be determined for all the $La_{1-x}Sr_xMnO_{2.5}$ phases studied.

The $C2/c$ structural model used to describe the $La_{1-x}Sr_xMnO_{2.5}$ $x = 0.2$, 0.25, and 0.3 phases is directly analogous to the structure refined previously for $La_{0.75}Sr_{0.25}MnO_{2.5}$ in the space group $P2_1/c$.[6] The additional symmetry operations present in the higher-symmetry $C2/c$ space group replace and replicate the additional symmetry which was added to the $P2_1/c$ model in the form of a large number of constraints applied to the atomic positional parameters. Utilizing a higher-symmetry space group, rather than adding constraints to parameters, is clearly a much more elegant way of describing the structure.

Table 1. Structural Parameters Refined against Neutron Powder Diffraction Data Collected from $La_{0.6}Sr_{0.4}MnO_{2.5}$[a]

atom	x	y	z	occupancy	U_{equiv} (Å^3)
La/Sr(1)	0.998(1)	0.3862(5)	0.2620(5)	0.6/0.4	0.0071(7)
La/Sr(2)	0.497(1)	0.8889(4)	0.5011(5)	0.6/0.4	0.0071(7)
Mn (1)	0.468(5)	0.25	0.222(2)	1	0.014(1)
Mn (2)	0.964(4)	0.25	0.026(2)	1	0.014(1)
Mn (3)	0	0	0	1	0.014(1)
Mn (4)	0.486(4)	0	0.25	1	0.014(1)
O (1)	0.940(3)	0.25	0.711(1)	1	0.015(1)
O (2)	0.257(2)	0.0084(7)	0.620(1)	1	0.015(1)
O (3)	0.981(2)	0.8645(7)	0.0257(9)	1	0.015(1)
O (4)	0.250(3)	0.0054(8)	0.122(2)	1	0.015(1)
O (5)	0.517(3)	0.3672(7)	0.2661(9)	1	0.015(1)
O (6)	0.575(3)	0.25	0.045(1)	1	0.015(1)

[a] Space group: *Pcmb*, $a = 5.4190(2)$ Å, $b = 16.6207(9)$ Å, $c = 11.0320(6)$ Å, cell volume = 993.6(1) Å^3; $wR_p = 3.82$ %, $R_p = 2.92$ %.

Table 2. Structural Parameters Refined against Neutron Powder Diffraction Data Collected from $La_{0.7}Sr_{0.3}MnO_{2.5}$[a]

atom	x (Å)	y (Å)	z (Å)	occupancy	U_{equiv} (Å^3)
La/Sr(1)	0.1112(4)	0.4900(9)	0.3171(4)	0.7/0.3	0.0052(4)
La/Sr(2)	0.3875(4)	0.493(1)	0.4462(4)	0.7/0.3	0.0052(4)
Mn (1)	0.5	0	0.5	1	0.0078(7)
Mn (2)	0	0.000(1)	0.25	1	0.0078(7)
Mn (3)	0.248(1)	0.462(1)	0.1492(6)	1	0.0078(7)
O (1)	0.9871(5)	0.251(2)	0.372(1)	1	0.0123(6)
O (2)	0.9914(6)	0.256(2)	0.873(1)	1	0.0123(6)
O (3)	0.1345(5)	0.015(1)	0.3394(7)	1	0.0160(7)
O (4)	0.3624(5)	0.015(1)	0.4622(7)	1	0.0160(7)
O (5)	0.2493(8)	0.5778(7)	0.3289(5)	1	0.017(1)

[a] Space group: $C2/c$, $a = 17.3667(8)$ Å, $b = 5.4660(1)$ Å, $c = 11.2087(3)$ Å, $\beta = 108.86(1)°$, cell volume = 1006.87(6) Å^3; $wR_p = 3.83\%$, $R_p = 2.96\%$.

Details of the refined structures of $La_{0.6}Sr_{0.4}MnO_{2.5}$ and $La_{0.7}Sr_{0.3}MnO_{2.5}$ are given in Tables 1 and 2. The refined structures of the remaining $La_{1-x}Sr_xMnO_{2.5}$ $x = 0.2$, 0.25, and 0.35 phases are given in the Supporting Information along with plots of the observed and calculated diffraction data for all $La_{1-x}Sr_xMnO_{2.5}$ phases. Selected bond lengths and angles from the refined structures of all the $La_{1-x}Sr_xMnO_{2.5}$ phases ($x = 0.2$, 0.25, 0.3, 0.35, 0.4) are listed in Table 3.

Structural Refinement of $La_{1-x}Ca_xMnO_{2.5}$ ($x = 0.4$, 0.35, 0.3, 0.25). The structures of $La_{1-x}Ca_xMnO_{2.5}$ phases were characterized utilizing neutron and electron diffraction data in a manner identical to that described for the $La_{1-x}Sr_xMnO_{2.5}$ above. Table S2 in the Supporting Information lists the fitting statistics for these refinements indicating *Pnma* ($x = 0.25$), $C2/c$ ($x = 0.3$) and *Pcmb* ($x = 0.35$, 0.4) structural variants are adopted by the calcium containing phases. Full details of the electron diffraction data collected from the $La_{1-x}Ca_xMnO_{2.5}$ phases, which agree with the structures refined from the neutron dif-

Table 4. Structural Parameters Refined against Neutron Powder Diffraction Data Collected from $La_{0.75}Ca_{0.25}MnO_{2.5}$[a]

atom	x	y	z	occupancy	U_{equiv} (Å^3)
La/Ca	0.4836(6)	0.1126(1)	0.0152(5)	0.75/0.25	0.0063(9)
Mn (1)	0	0	0	1	0.004(1)
Mn (2)	0.453(2)	0.25	0.551(1)	1	0.004(1)
O (1)	0.2696(8)	0.9851(2)	0.2258(8)	1	0.012(1)
O (2)	0.0257(8)	0.1371(2)	0.0730(6)	1	0.015(1)
O (3)	0.572(1)	0.25	0.902(1)	1	0.016(2)

[a] Space group: *Pnma*, $a = 5.4901(4)$ Å, $b = 16.140(1)$ Å, $c = 5.6477(4)$ Å, cell volume = 500.43(8) Å^3; $wR_p = 6.03$ %, $R_p = 4.81$ %.

Table 3. Selected Bond Lengths (Å) and Angles (deg) from the Refinement of $La_{1-x}Sr_xMnO_{2.5}$ Phases

$La_{1-x}Sr_xMnO_{2.5}$		$x = 0.2$	$x = 0.25$	$x = 0.3$		$x = 0.35$	$x = 0.4$
Mn octahedral	Mn(1)−O(1)×2	1.945(5)	1.928(7)	1.93(1)	Mn(3)−O(2)×2	1.96(1)	1.92(1)
	Mn(1)−O(2)×2	1.959(4)	1.910(8)	1.92(1)	Mn(3)−O(4)×2	1.95(1)	1.91(1)
	Mn(1)−O(4)×2	2.293(5)	2.291(8)	2.29(1)	Mn(3)−O(3)×2	2.25(1)	2.27(1)
	BVS	3.09	3.33	3.29	BVS	3.13	3.40
Mn octahedral	Mn(2)−O(1)×2	2.034(5)	2.03(1)	2.00(1)	Mn(4)−O(2)×2	1.94(2)	2.00(1)
	Mn(2)−O(2)×2	2.007(4)	2.04(1)	2.00(1)	Mn(4)−O(4)×2	1.93(1)	1.90(2)
	Mn(2)−O(3)×2	2.21(1)	2.24(1)	2.22(1)	Mn(4)−O(5)×2	2.22(1)	2.22(1)
	BVS	2.78	2.65	2.89	BVS	3.31	3.24
Mn tetrahedral	Mn(3)−O(3)	1.988(6)	1.96(1)	2.02(1)	Mn(1)−O(1)	2.14(2)	2.21(3)
	Mn(3)−O(4)	1.98(1)	2.00(1)	1.94(1)	Mn(1)−O(6)	2.06(1)	2.03(2)
	Mn(3)−O(5)	2.092(2)	2.09(1)	2.10(1)	Mn(1)−O(5)×2	2.02(1)	2.02(1)
	Mn(3)−O(5)	2.151(2)	2.119(6)	2.113(7)			
	BVS	2.00	2.05	2.05	BVS	1.94	1.91
Mn tetrahedral					Mn(2)−O(1)	2.13(1)	2.10(2)
					Mn(2)−O(6)	2.08(2)	2.12(2)
					Mn(2)−O(3)×2	2.00(1)	2.00(1)
					BVS	**1.98**	**1.97**
tetrahedral twist	O(5)−O(5)−O(5)	116.22(4)	115.3(1)	113.9(1)	O(1)−O(6)−O(1)	112.6(5)	111.8(6)
layer separation		8.14(2)	8.16(2)	8.21(2)		8.262(1)	8.310(1)

Table 5. Selected Bond Lengths (Å) and Angles (deg) from the Refinement of $La_{1-x}Ca_xMnO_{2.5}$ Phases

$La_{1-x}Ca_xMnO_{2.5}$		$x = 0.25$		$x = 0.3$		$x = 0.35$	$x = 0.4$
Mn octahedral	Mn(1)−O(1)×2	2.014(4)	Mn(1)−O(1)×2	1.930(7)	Mn(3)−O(2)×2	1.925(9)	1.97(1)
	Mn(1)−O(1)×2	1.968(4)	Mn(1)−O(2)×2	1.941(8)	Mn(3)−O(4)×2	1.975(9)	1.909(9)
	Mn(1)−O(2)×2	2.255(3)	Mn(1)−O(4)×2	2.275(7)	Mn(3)−O(3)×2	2.24(1)	2.24(1)
	BVS	2.89	BVS	3.24	BVS	3.21	3.27
Mn octahedral			Mn(2)−O(1)×2	2.03(1)	Mn(4)−O(2)×2	2.03(2)	1.89(2)
			Mn(2)−O(2)×2	1.99(1)	Mn(4)−O(4)×2	1.93(1)	2.09(2)
			Mn(2)−O(3)×2	2.201(6)	Mn(4)−O(5)×2	2.25(1)	2.23(1)
			BVS	2.87	BVS	2.99	3.02
Mn tetrahedral	Mn(2)−O(3)	2.11(1)	Mn(3)−O(3)	1.98(1)	Mn(1)−O(1)	2.18(2)	2.20(3)
	Mn(2)−O(3)	2.087(9)	Mn(3)−O(4)	1.99(1)	Mn(1)−O(6)	2.02(3)	2.00(2)
	Mn(2)−O(2)×2	1.993(4)	Mn(3)−O(5)	2.137(6)	Mn(1)−O(5)×2	1.99(1)	2.02(1)
			Mn(3)−O(5)	2.080(9)			
	BVS	2.02	BVS	2.02	BVS	2.05	1.97
Mn tetrahedral					Mn(2)−O(1)	2.10(2)	2.11(2)
					Mn(2)−O(6)	2.08(2)	2.25(2)
					Mn(2)−O(3)×2	1.97(1)	1.96(1)
					BVS	2.11	1.97
tetrahedral twist	O(2)−O(2)−O(2)	116.0(2)	O(5)−O(5)−O(5)	115.0(1)	O(1)−O(6)−O(1)	114.4(5)	112.8(6)
layer separation		8.070(1)		8.066(1)		8.103(1)	8.166(1)

Table 6. Structural Parameters Refined against Neutron Powder Diffraction Data Collected from $La_{0.8}Ba_{0.2}MnO_{2.5}$[a]

atom	x (Å)	y (Å)	z (Å)	occupancy	U_{equiv} (Å^3)
La/Ba	0.487(4)	0.1131(1)	0.0095(6)	0.8/0.2	0.0099(8)
Mn (1)	0	0	0	1	0.006(2)
Mn (2)	0.968(4)	0.75	0.044(1)	1	0.011(2)
O (1)	0.234(4)	0.9893(3)	0.258(2)	1	0.018(1)
O (2)	0.961(3)	0.1372(2)	0.0559(7)	1	0.028(1)
O (3)	0.576(3)	0.75	0.106(1)	1	*Anisotropic*

[a] O(3) displacement ellipsoids: $U_{11} = 0.087(8)$, $U_{22} = 0.028(5)$, $U_{33} = 0.054(5)$, $U_{13} = 0.051(5)$. Space group : *I2mb*, $a = 5.5591(3)$ Å, $b = 16.3997(9)$ Å, $c = 5.6666(3)$ Å, cell volume = 516.59(7) Å^3; $wR_p = 5.54$ %, $R_p = 4.32$ %.

fraction data, are given in the Supporting Information. Details of the refined structure of $La_{0.75}Ca_{0.25}MnO_{2.5}$ are given in Table 4. The refined structures of the remaining $La_{1-x}Ca_xMnO_{2.5}$ ($x = 0.3$, 0.35, and 0.4) phases are given in the Supporting Information along with plots of the observed and calculated diffraction data for all $La_{1-x}Ca_xMnO_{2.5}$ phases. Selected bond lengths and angles from the refined structures of all the $La_{1-x}Ca_xMnO_{2.5}$ phases ($x = 0.25$, 0.3, 0.35, 0.4) are listed in Table 5.

Structural Refinement of $La_{1-x}Ba_xMnO_{2.5}$ ($x = 0.3$, 0.25, 0.2, 0.167). Models based on the five variants of the brownmillerite structure, described above, were refined against neutron powder diffraction data collected from $La_{1-x}Ba_xMnO_{2.5}$ samples. It can be seen from the fitting statistics in Table S3 (see the Supporting Information) that $La_{1-x}Ba_xMnO_{2.5}$ phases adopt either *I2mb* ($x = 0.166$, 0.2) or *C*2/*c* ($x = 0.25$, 0.3) structural variants. Close inspection of the *I2mb* structural models refined for $x = 0.166$ and 0.2 samples revealed the displacement ellipsoids for the equatorial oxide ions in the tetrahedral layers (O3) were much larger than those of any of the other oxide ions. An anisotropic description of this displacement was adopted leading to a significant improvement to the fits (see Table S3 in the Supporting Information). The largest value of the refined anisotropic displacement is in a direction almost perpendicular to the Mn−O−Mn bond vector suggesting it is modeling a small amount of disorder in the tetrahedral twist direction; however, this "anisotropic *I2mb*" model is a better statistical fit than the fully disordered Imma model.

To investigate this disorder and confirm the symmetry of all the $La_{1-x}Ba_xMnO_{2.5}$ phases, electron diffraction data were collected from the $x = 0.25$ and $x = 0.2$ samples are consistent with the *C*2/*c* structural variant (see the Supporting Information). The data collected from the $x = 0.166$ and $x = 0.2$ samples can be indexed with body-centered cells indicating *I2mb* or *Imma* structures. However, both samples exhibited diffuse intensity in the diffraction data collected that is consistent with small domains of intralayer order (*C*2/*c*, *Pcmb* or the more complex order described in ref 4). These observations are consistent with the disorder observed via neutron diffraction. On balance, it was decided to retain the *I2mb* description of the $x = 0.166$ and $x = 0.2$ phases but with the comment that both phases contained small domains or intergrowths of intralayer ordered structural variants.

Details of the refined structure of $La_{0.8}Ba_{0.2}MnO_{2.5}$ are given in Table 6. The refined structures of the remaining $La_{1-x}Ba_xMnO_{2.5}$ ($x = 0.166$, 0.25, and 0.3) phases are given in the supporting information along with plots of the observed and calculated diffraction data for all $La_{1-x}Ba_xMnO_{2.5}$ phases. Selected bond lengths and angles from the refined structures of all the $La_{1-x}Ba_xMnO_{2.5}$ phases ($x = 0.166$, 0.2, 0.25, 0.3) are listed in Table 7.

Neutron diffraction data collected at 5 K from all $La_{1-x}A_xMnO_{2.5}$ (A = Ba, Sr, Ca) samples exhibited additional diffraction features, compared to analogous room temperature data sets, indicative of magnetic order. The complex evolution of the magnetic behavior of these phases as a function of composition and temperature will be described elsewhere.

Discussion

Thermogravimetric and diffraction data show that all the $La_{1-x}A_xMnO_{2.5}$ (A = Ba, Sr, Ca) phases described above adopt brownmillerite-type anion vacancy ordered structures. The identity of the different brownmillerite

Table 7. Selected Bond Lengths (Å) and Angles (deg) from the Refinement of $La_{1-x}Ba_xMnO_{2.5}$ Phases

$La_{1-x}Ba_xMnO_{2.5}$		$x = 0.166$	$x = 0.2$		$x = 0.25$	$x = 0.3$
Mn octahedral	Mn(1)−O(1)×2	2.02(2)	2.02(1)	Mn(1)−O(1)×2	2.02(1)	2.03(1)
	Mn(1)−O(1)×2	1.97(2)	1.97(2)	Mn(1)−O(2)×2	2.06(1)	2.05(1)
	Mn(1)−O(2)×2	2.269(4)	2.283(4)	Mn(1)−O(4)×2	2.28(1)	2.33(1)
	BVS	2.85	2.84	BVS	2.57	2.50
Mn octahedral				Mn(2)−O(1)×2	1.94(2)	1.93(1)
				Mn(2)−O(2)×2	1.94(2)	1.92(1)
				Mn(2)−O(3)×2	2.28(1)	2.26(1)
				BVS	3.19	3.19
Mn tetrahedral	Mn(2)−O(2)×2	1.939(4)	1.935(4)	Mn(3)−O(3)	1.96(3)	2.02(2)
	Mn(2)−O(3)	2.08(1)	2.07(1)	Mn(3)−O(4)	2.00(3)	1.93(2)
	Mn(2)−O(3)	2.24(3)	2.21(3)	Mn(3)−O(5)	2.08(1)	2.09 (1)
				Mn(3)−O(5)	2.139(9)	2.11(1)
	BVS	2.09	2.14	BVS	2.04	2.08
tetrahedral twist	O(3)−O(3)−O(3)	119.2(6)	119.2(6)	O(5)−O(5)−O(5)	117.3(2)	116.7(2)
layer separation		8.177(1)	8.199(1)		8.23(2)	8.28(2)

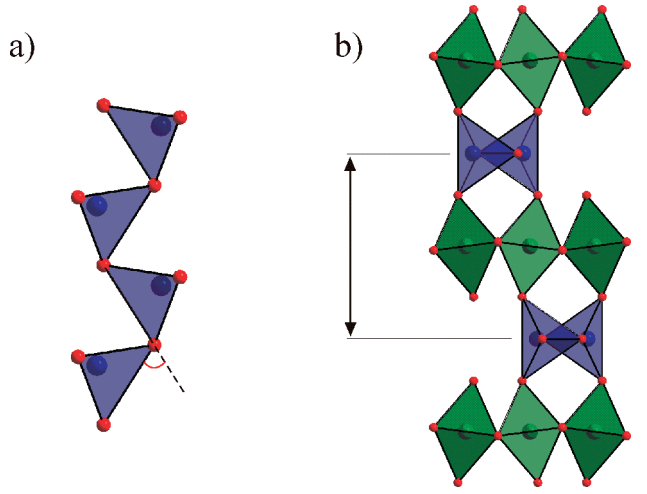

Figure 6. (a) Tetrahedral O−O−O distortion angle; (b) tetrahedral layer separation.

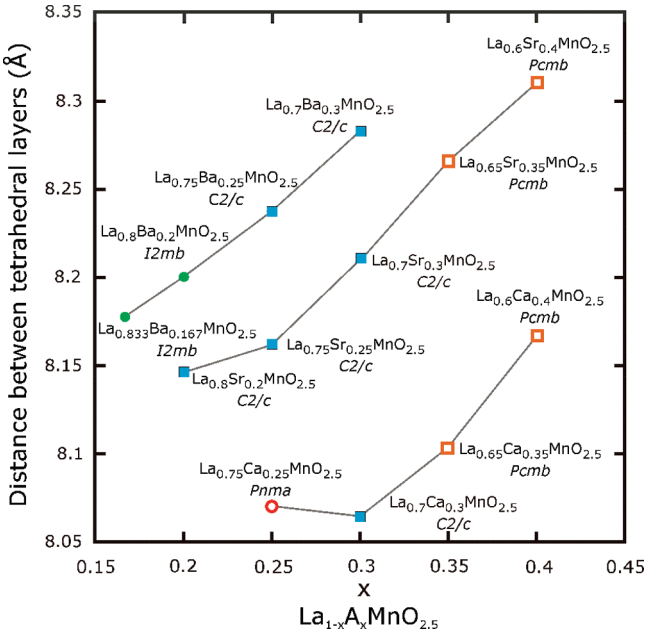

Figure 7. Plot of the layer separation against composition for $La_{1-x}A_x$-$MnO_{2.5}$ phases.

structural variants adopted by $La_{1-x}A_xMnO_{2.5}$ phases as a function of chemical composition is shown in Figure 3. As noted above, a complete analysis of the influences which direct the brownmillerite structural variant adopted by a particular chemical composition, has been hampered by a lack of accurate structural parameters (bond lengths and angles) for phases with the C2/c and Pcmb structure types. The structural refinement of $La_{1-x}A_xMnO_{2.5}$ phases above, has yielded the first (to the best of our knowledge) accurate structural parameters for a Pcmb brownmillerite phase and has clarified and added to the only set of *C*2/*c* brownmillerite parameters reported.[6] These new structural data allow the detailed analysis of the brownmillerite series of structures for the first time. As detailed below, we will focus on a number of structural parameters, most notably the tetrahedral chain distortion (Figure 6a) and the interlayer separation (Figure 6b), to rationalize the brownmillerite structural family.

Interlayer Separation. Figure 7 shows a plot of the separation between tetrahedral layers in the $La_{1-x}A_x$-$MnO_{2.5}$ (A = Ba, Sr, Ca) phases prepared in this study, against x the La:A cation ratio. These data reveal that for a given value of *x*, the size of the interlayer separation is always in the order A = Ba > Sr > Ca as would be expected on the basis of the ionic radii of the A-cations. Further inspection of the data reveals that with the exception of $La_{0.75}Ca_{0.25}MnO_{2.5}$, which will be discussed in detail later, the interlayer separation increases fairly steadily with increasing *x* in all three compositional series. This increase can be rationalized by considering the change in the manganese oxidation state with *x*. Bond valence sums (BVS)[22] calculated for all the brownmillerite phases considered (Tables 3, 5 and 7) reveal that the tetrahedral sites in these structures are occupied by Mn(II). This implies that the manganese centers in the octahedral sites have average manganese oxidation states which vary, as a function of x, between Mn +2.33 ($x = 0.167$) and Mn +2.8 ($x = 0.4$). The increase in interlayer separation with increasing x can be rationalized on the basis of an increasing concentration of Jahn−Teller distorted Mn(III) centers on the octahedral sites, which have extended axial Mn−O bonds. This extension forces the

(22) Brese, N. E.; O'Keefe, M. *Acta Crystallogr., Sect. B* **1991**, *B47*, 192–197.

Table 8. Octahedral Bond Lengths (Å) Extracted from the Refined Structures of $La_{1-x}A_xMnO_{2.5}$ Phases

	$La_{1-x}Ba_xMnO_{2.5}$			$La_{1-x}Sr_xMnO_{2.5}$			$La_{1-x}Ca_xMnO_{2.5}$		
x	Mn−O eq	Mn−O ax	ax/eq	Mn−O eq	Mn−O ax	ax/eq	Mn−O eq	Mn−O ax	ax/eq
0.166	1.995(20)	2.269(4)	1.137(13)						
0.2	1.995(15)	2.283(4)	1.144(10)	1.986(4)	2.251(8)	1.133(6)			
0.25	1.990(15)	2.280(10)	1.145(13)	1.977(8)	2.265(4)	1.145(6)	1.991(4)	2.255(3)	1.132(2)
0.3	1.982(10)	2.295(10)	1.157(7)	1.962(10)	2.255(10)	1.149(11)	1.972(8)	2.238(6)	1.134(7)
0.35				1.945(12)	2.235(10)	1.149(12)	1.965(7)	2.245(10)	1.142(9)
0.4				1.932(12)	2.245(10)	1.162(12)	1.964(14)	2.235(10)	1.137(13)

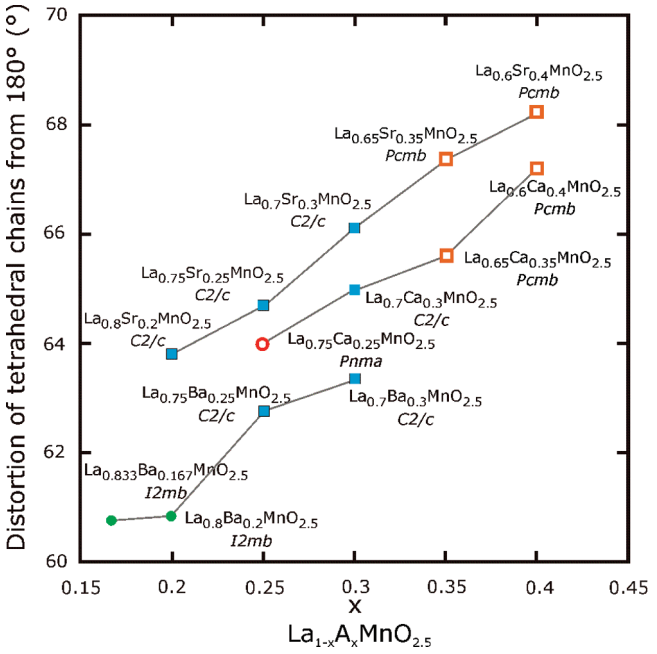

Figure 8. Plot of the tetrahedral chain distortion against composition for $La_{1-x}A_xMnO_{2.5}$ phases.

tetrahedral layers apart as x is increased. Table 8 lists the axial and equatorial Mn−O bond lengths for the octahedral sites in all the $La_{1-x}A_xMnO_{2.5}$ phases studied. It is clear that (with the exception of $La_{0.6}Ca_{0.4}MnO_{2.5}$) the ratio of the axial/equatorial bond lengths increases with increasing x for all three compositional series, further supporting the idea that it is the extent of the distortion of the octahedral sites which controls the interlayer separation in these phases by opposing the contractive effects imposed by the A-cation site.

Tetrahedral Chain Distortion. It can be seen that the degree of distortion of the tetrahedral chains in the $La_{1-x}A_xMnO_{2.5}$ phases (Figure 8) increases steadily with increasing A-cation concentration (x). This can again be rationalized by observing that the average oxidation state of the manganese centers located on the octahedral sites increases with increasing x. As the concentration of Mn(III) increases there is a contraction of the in-plane Mn−O bonds of these octahedra which drives a general contraction of the structural plane perpendicular to the octahedral-tetrahedral stacking direction. This contraction can be clearly seen in the equatorial Mn−O bond lengths and lattice parameters in Table 8 and the Supporting Information. The contraction of the octahedral sheets with increasing x, forces the tetrahedral centers closer together driving the increased twisting of the tetrahedral chains observed.

Structure Compositional Relations. Abakumov et al.[7] and Hadermann et al.[8] have presented a rationalization for the formation of the *I2mb* and *Pnma* brownmillerite structural variants based on the compensation of dipole moments. As shown in Figure 2, each of the MnO_4 tetrahedra exhibit an in-plane dipole moment. When the tetrahedral chains twist, the dipole moments on neighboring tetrahedra no longer cancel leading to a net dipole moment along each tetrahedral chain. The adoption of different brownmillerite structure types is driven by the need to minimize the net dipole moment exhibited. When the dipole moment of each chain is small, as measured by the angle of the tetrahedral chain distortion, the noncentric *I2mb* structural variant is adopted in which all tetrahedral chains twist in the same direction (Figure 1). This leads to a polar structure with a local net dipole moment. Compensation of this dipole moment is achieved by the formation of small ferroelectric domains, the polarization vectors of which are aligned in an antiparallel manner resulting in no net macroscopic dipole. As the distortion of the tetrahedral chains and thus their dipole moment increases, the micro-domain method of dipole cancellation is replaced by an interlayer cancellation scheme associated with the adoption of the Pnma structural variant. In this structure, the tetrahedral twist direction inverts between adjacent tetrahedral layers (Figure 1) resulting in a dipole cancellation between equally but oppositely twisted tetrahedral chains. When the separation between tetrahedral layers becomes large however, this interlayer compensation becomes weak and an intralayer dipole cancellation scheme becomes favorable, leading to the adoption of the *C*2/*c* and Pcmb structure types observed in the $La_{1-x}A_xMnO_{2.5}$ (A = Ba, Sr, Ca) compositional series. In these two structural variants the twist direction of the tetrahedral chains alternates within each tetrahedral layer (Figure 1) resulting in dipole cancellation.

The fact that brownmillerite structures adopt a number of different dipole cancellation schemes, rather than one universal "best method" of dipole cancellation, indicates that the structural variants adopted are a compromise between competing influences. Abakumov et al. observed that different tetrahedral chain twist patterns induce different tilting patterns into the intervening octahedral layers, which have potentially undesirable consequences for the overall lattice energy of structures.[7] Here we present a modified and extended version of this argument.

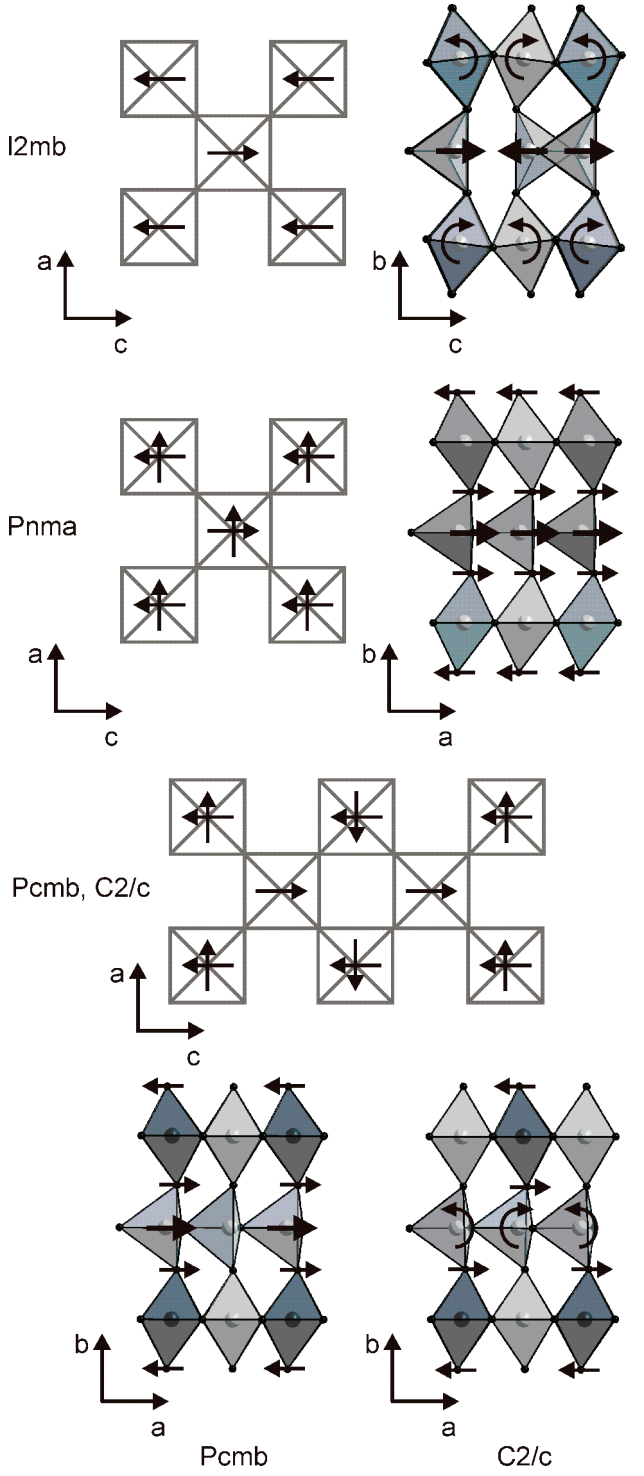

Figure 9. Ordered tilting and distortion modes of the octahedral layers within brownmillerite structures.

The simplest brownmillerite structural variant (*I2mb*) has a uniform twist direction of the tetrahedral chains which induces a simple alternating 1D tilt into the octahedral layers parallel to the *c*-axis (Figure 9). The direction of the tilt is inverted between adjacent layers such that the BO_4 tetrahedra, which link the octahedral layers, undergo a simple alternating 1D translation parallel to the *c*-axis because of the octahedral tilt. This tilting of the octahedra in the *bc* plane is observed in all the brownmillerite structural variants discussed. When the Pnma structural variant is adopted however, the inversion of the tetrahedral twist direction between adjacent layers induces a further component to the displacement of the axial anion positions parallel to the *a*-axis. This additional displacement is uniform in direction and so distorts the octahedral sites rather than tilting them. The combined 2D displacement of the axial anions in the *ac* plane leads to a 2D ordered translation of the intervening BO_4 tetrahedra, which disrupts the $La_{1-x}A_x$-O layers, destabilizing the structure. The ordered intralayer alternation of the tetrahedral twist direction observed in the *Pcmb* and *C*2/*c* structural variants induces a more complex octahedral tilt/distortion pattern in which half the octahedra are tilted in 1D and half are tilted/distorted in 2D (Figure 9). The *Pcmb* structural variant stacks these octahedral sheets in an "eclipsed" manner which results in two crystallographically distinct tetrahedral sites; one translated in 1D parallel to the *a*-axis, one translated in 2D within the *ac* plane. The *C*2/c structural variant stacks the octahedral sheets in a "staggered" manner such that each BO_4 tetrahedron shares one apical oxide ion with an octahedron tilted in 1D and one tilted/distorted in 2D. This induces a tilt as well as a shift into the tetrahedral layers further disrupting the structure. It can therefore be seen that the degree of structural disruption induced by the different tetrahedral twist patterns follows the order *I2mb* < *Pnma* < *Pcmb* < *C*2/*c* and that the more disrupted structures are only adopted when the chain dipole moments become too large, or the tetrahedral layers too far apart, for effective dipole cancellation with less disrupted structures.

Figure 10 shows a plot of the tetrahedral chain distortion against tetrahedral layer separation of the $La_{1-x}A_xMnO_{2.5}$ phases prepared in this study. It can be seen that the brownmillerite structural variants adopted by these phases agree well with the rationalization described above. At small tetrahedral chain distortions the *I2mb* structure type is adopted. As the tetrahedral chain distortion increases there is a change to the *C*2/*c* and *Pcmb* structure types at large layer separation and the *Pnma* structural variant at small layer separations.

Octahedral Site Charge Order. The above rationalization does not explain the existence of the *C*2/*c* structural variant, given that it appears to have the same dipole cancellation method as the Pcmb variant but greater structural disruption. It has been observed previously that $La_{1-x}A_xMnO_{2.5}$ phases which adopt the *C*2/*c* brownmillerite structure exhibit charge ordering between Mn(II) and Mn(III) centers within their octahedral layers.[6] Examination of the phases prepared in this study that exhibit the *C*2/*c* structural variant (Tables 3, 5 and 7) reveals that there are large differences between the bond valence sums observed for the two crystallographically distinct octahedral sites in *C*2/*c* structures (ΔBVS = 0.32−0.68) compared to those of the *Pcmb* type structures ($\Delta BVS = 0.16-0.25$). In addition, it can be seen that the sites with the higher calculated BVS have much larger axial/equatorial bond length ratios than the "lower BVS" octahedral sites. These observations are consistent with

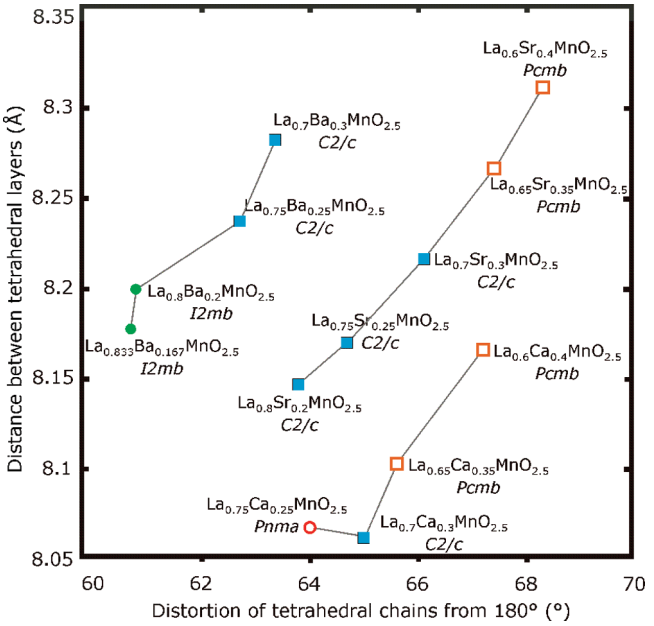

Figure 10. Plot of the tetrahedral chain distortion against the layer separation for the $La_{1-x}A_xMnO_{2.5}$ phases.

the presence of "small" Jahn−Teller distorted Mn(III) centers ordered with "large" less distorted Mn(II) centers and thus support the presence of charge ordering in the octahedral sites of all phases adopting the *C*2/*c* structural variant. The observation that all the phases that adopt the *C*2/*c* structure are charge ordered strongly suggests the *C*2/*c* structural variant is able to stabilize octahedral site charge ordering and is the preferred structural variant when charge ordering is sufficiently energetically advantageous ($x \approx 0.25$) so as to overcome the additional disruption induced into the $La_{1-x}A_x$−O framework.

The stabilization of the octahedral site charge order by the *C*2/*c* structural variant can be seen to derive from the stacking of the ordered octahedral sheets (Figure 11). As noted previously, the difference between the *C*2/*c* and *Pcmb* structural variants derives from the adoption of different tetrahedral layer stacking sequences − AAAA for *C*2/*c*, ABAB for *Pcmb*. These stacking sequences also affect the octahedral layers. The octahedral layers in both the Pcmb and *C*2/*c* structural variants contain two distinct octahedral centers, arranged in the chequerboard pattern within each layer. The ABAB stacking sequence of the Pcmb structure leads to a simple primitive stacking of the octahedral layers, with like octahedral centers stacked in an "eclipsed" manner directly on top of each other (Figures 1 and 11). The AAAA stacking of the *C*2/*c* structural variant leads to an arrangement in which the octahedral layers are stacked in a staggered manner with unlike octahedra on top of each other (Figures 1 and 11). As noted previously, the Mn(III) centers located within octahedral sites exhibit extended axial Mn−O bond lengths associated with the Jahn−Teller distortion of a d^4 center. In the Pcmb structural variant these extended bonds are stacked in a primitive manner leading to significant strain from the opposed extensions (Figure 11). In the *C*2/*c* structure, the staggered stacking of the charge

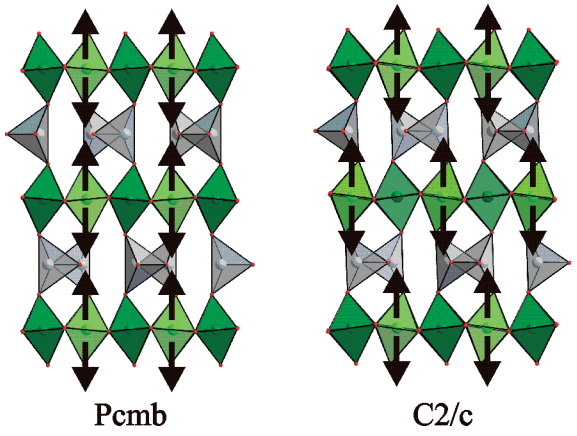

Figure 11. Disposition of the Jahn−Teller distorted Mn(III) centers when charge-ordered within the *Pcmb* and *C*2/*c* brownmillerite structural variants.

ordered layers relieves this strain, explaining the preference for this structural variant in the presence of charge ordering.

Structure of $La_{0.75}Ca_{0.25}MnO_{2.5}$. The structure of $La_{0.75}Ca_{0.25}MnO_{2.5}$ appears to be anomalous. Despite possessing a La:Ca stoichiometric ratio which leads to a 1:1 ratio of Mn(III):Mn(II) centers within the octahedral sites of the phase (the optimal ratio for charge ordering) $La_{0.75}Ca_{0.25}MnO_{2.5}$ adopts the Pnma structural variant, incompatible with long range charge order. Indeed, close inspection of this phase utilizing both neutron and electron diffraction yields no evidence for even short range charge order−a surprise given the strongly charge ordered structures observed for $La_{0.7}Ca_{0.3}MnO_{2.5}$ and $La_{0.75}Sr_{0.25}MnO_{2.5}$.

Examining the structural details of $La_{0.75}Ca_{0.25}MnO_{2.5}$ provides some explanation. It can be seen from Figure 8 that the tetrahedral chain twisting angle of $La_{0.75}Ca_{0.25}MnO_{2.5}$ is intermediate between those observed for the strongly charge ordered phases $La_{0.75}Sr_{0.25}MnO_{2.5}$ and $La_{0.75}Ba_{0.25}MnO_{2.5}$. This indicates that the tetrahedral chain dipole moment present in $La_{0.75}Ca_{0.25}MnO_{2.5}$ is sufficient to induce an intralayer Pcmb or C2/c structure type. The interlayer separation observed for $La_{0.75}Ca_{0.25}MnO_{2.5}$, however, appears to be anomalously large when compared to other $La_{1-x}Ca_xMnO_{2.5}$ phases. Figure 7 shows that the interlayer separation decreases almost linearly with decreasing x in the $La_{1-x}Ca_xMnO_{2.5}$ structural series. Extrapolating this trend yields an interlayer separation of ~8.01 Å for $La_{0.75}Ca_{0.25}MnO_{2.5}$ rather than the 8.07 Å distance observed. As noted above the interlayer separation is determined by the competition between the La/A cation coordination site which acts to contract the structure and the axial bond of the MnO_6 octahedral sites which acts to expand the structure. As the interlayer separation contracts with decreasing x, the structural strain induced by this competition rises. If $La_{0.75}Ca_{0.25}MnO_{2.5}$ adopted a structure with an interlayer separation of 8.01 Å this would require a significant compression of the octahedral site axial bond lengths and/or an extreme tilting/distortion of the MnO_6

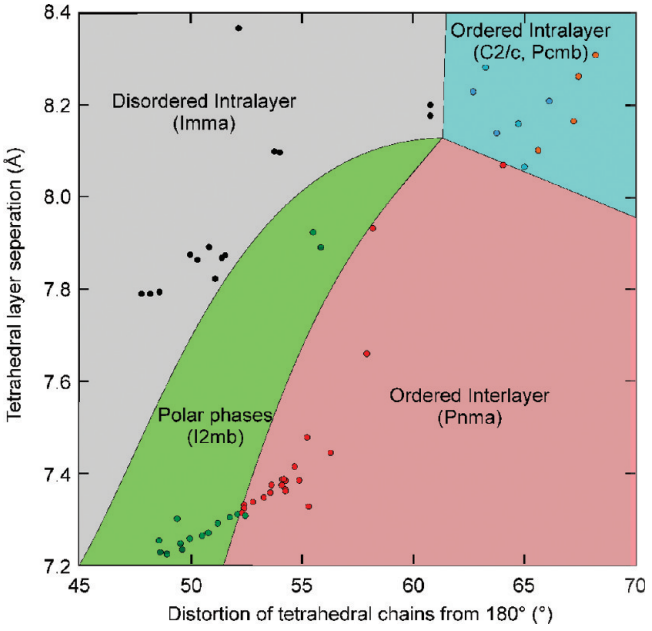

Figure 12. Brownmillerite structure map as a function of interlayer separation and tetrahedral chain distortion.

octahedra in order to fit them into the axially compressed structure. The observation that $La_{0.75}Ca_{0.25}MnO_{2.5}$ adopts the larger interlayer separation of 8.07 Å indicates that the increased strain associated with these structural distortions is unfavorable. Furthermore the adoption of the Pnma structural variant by $La_{0.75}Ca_{0.25}MnO_{2.5}$, rather then the *C*2/*c* or *Pcmb* variants, suggests that the compression of the structure increases the energetic penalty associated with the more structurally disruptive octahedral tilting patterns in the latter structures, driving $La_{0.75}Ca_{0.25}MnO_{2.5}$ to adopt the Pnma structural arrangement. Thus it can be seen that the contraction of the interlayer separation forces $La_{0.75}Ca_{0.25}MnO_{2.5}$ to adopt the Pnma structural variant.

Brownmillerite Structure Map. To asses how widely the structural arguments outlined above can be applied, a wide variety of phases exhibiting brownmillerite structures were added to the plot of tetrahedral chain distortion against interlayer separation as shown in Figure 12.

A full list of the phases contributing to Figure 12 is given in the Supporting Information.[9,23−46]

The data in Figure 12 agree very well with structural arguments detailed above and outline a "structure map" for brownmillerite-type structures. When the interlayer separation is small ($b/2 < 7.6$ Å) there is a steady progression from polar I2mb to interlayer ordered Pnma structural variants with increasing tetrahedral chain distortion (dipole moment). As the interlayer separation grows ($7.6 < b/2$(Å) < 8) disordered structures (*Imma*) are observed when the tetrahedral chain distortion is small, with the same progression to polar and interlayer ordered structures with increasing chain distortion, as observed at smaller layer separations. At large interlayer separation ($b/2 > 8$ Å) disordered structures are still present at small chain distortions, but there is a change to intralayer ordered structures (*C*2/*c*, *Pcmb*) at large tetrahedral chain distortions. This is consistent with the reduced effectiveness of interlayer dipole compensation at large interlayer separations leading to the adoption of intralayer dipole compensation.

The structural disorder in the "*Imma* region" of Figure 12 could exist in a number of forms: (i) the arrangement of tetrahedral chain twist directions could simply be random (disordered); (ii) layers with a uniform twist direction could be stacked in a disordered way (rather than the ordered manner observed in the Pnma structural variant). Thus we would have interlayer dipole compensation but no overall structural order (disordered interlayer); (iii) there could be rigorous alternation of the chain twist direction within the tetrahedral layers (as observed for the *C*2/*c* and *Pcmb* variants) but a disordered stacking of these layers. Thus we would have intralayer dipole compensation but an overall disordered structure (disordered intralayer). Whatever the exact nature of the structural disorder in the "*Imma*" phases in Figure 12, the observation that disordered structures occur at small

(23) Redhammer, G. J.; Tippelt, G.; Roth, G.; Amthauer, G. *Am. Mineral.* **2004**, *89*, 405–420.
(24) Colville, A. A.; Geller, S. *Acta Crystallogr., Sect. B* **1971**, *27*, 2311–2315.
(25) Colville, A. A.; Geller, S. *Acta Crystallogr., Sect. B* **1972**, *28*, 3196–3200.
(26) Jupe, A. C.; Cockroft, J. K.; Barnes, P.; Colston, S. L.; Sankar, G.; Hall, C. *J. Appl. Crystallogr.* **2001**, *34*, 55–61.
(27) Luzikova, A. V.; Karlanov, A. L.; Antipov, E. V.; Mueller-Buschbaum, H. *Z. Anorg. Allg. Chem.* **1994**, *620*, 326–328.
(28) Kahlenberg, V.; Fischer, R. X. *Eur. J. Mineral.* **2000**, *12*, 129–135.
(29) Arpe, R.; von Schenk, R.; Mueller-Buschbaum, H. *Z. Anorg. Allg. Chem.* **1974**, *410*, 97–103.
(30) Colville, A. A. *Acta Crystallogr., Sect. B* **1970**, *26*, 1469–1473.
(31) Berastegui, P.; Eriksson, S. G.; Hull, S. *Mater. Res. Bull.* **1999**, *34*, 303–314.
(32) Ramezanipour, R.; Cowie, B.; Derakhshan, S.; Greedan, J. E.; Cranswick, L. M. D. *J. Solid State Chem.* **2009**, *182*, 153–159.
(33) Harringer, N. A.; Presslinger, H.; Klepp, K. O. *Z. Kristallogr.* **2004**, *219*, 5–6.
(34) Istomin, S. Y.; Abdyusheva, S. V.; Svenson, G.; Antipov, E. V. *J. Solid State Chem.* **2004**, *177*, 4251–4257.
(35) Battle, P. D.; Gibb, T. C.; Lightfoot, P. *J. Solid State Chem.* **1988**, *76*, 334–339.
(36) Harrison, W. T. A.; Lee, T. H.; Yang, Y. L.; Scarfe, D. P.; Liu, L. M.; Jacobson, A. J. *Mater. Res. Bull.* **1995**, *30*, 621–630.
(37) Streule, S.; Medarde, M.; Podlesnyak, A.; Pomjakushina, E.; Conder, K.; Kazakov, S.; Karpinski, J.; Mesot, J. *Phys. Rev. B* **2006**, *73*, 24423-1–24423-8.
(38) Lindberg, F.; Istomin, S. Y.; Berastegui, P.; Svenson, G.; Kazakov, S. M.; Antipov, E. V. *J. Solid State Chem.* **2003**, *173*, 395–406.
(39) Harder, M.; Mueller-Buschbaum, H. *Z. Anorg. Allg. Chem.* **1980**, *464*, 169–175.
(40) Greaves, C.; Jacobson, A. J.; Tofield, B. C.; Fender, B. E. F. *Acta Crystallogr., Sect. B* **1975**, *31*, 641–646.
(41) Schmidt, M.; Campbell, S. J. *J. Solid State Chem.* **1999**, *156*, 292–304.
(42) Hodges, J. P.; Short, S.; Jorgensen, J. D.; Xiong, X.; Dabrowski, B.; Mini, S. M.; Kimball, C. W. *J. Solid State Chem.* **2000**, *151*, 190–209.
(43) Pomjakushin, V. Y.; Balagurov, A. M.; Elzhov, T. V.; Sheptyakov, D. V.; Fischer, P.; Khomskii, D. I.; Yushankhai, V. Y.; Abakumov, A. M.; Rozova, M. G.; Antipov, E. V.; Lobanov, M. V.; Billinge, S. J. L. *Phys. Rev. B* **2002**, *66*, 184412.
(44) Sheptyakov, D. V.; Abakumov, A. M.; Antipov, E. V.; Balagurov, A. M.; Billinge, S. J. L.; Fischer, P.; Keller, L.; Lobanov, M. V.; Pavlyuk, B. P.; Pomjakushin, V. Y.; Rozova, M. G. *Appl. Phys. A* **2002**, *74*, S1734–S1736.
(45) Berastegui, P.; Hull, S.; Garcia-Garcia, F. J.; Eriksson, S. G. *J. Solid State Chem.* **2002**, *164*, 119–130.
(46) Munoz, A.; de La Calle, C.; Alonso, J. A.; Botta, P. M.; Pardo, V.; Baldomir, D.; Rivas, J. *Phys. Rev. B* **2008**, *74*, 55404.

tetrahedral chain distortions is consistent with the thought that small tetrahedral chain dipole moments will have insufficient influence to overcome competing local factors and induce long-range structural order.

It is likely that different combinations of order and disorder are present in phases which occupy different areas of the "disordered region" of Figure 12. For example, we might expect disordered intralayer structures to be adopted by phases with large interlayer separations, by analogy to the ordered phases. Considering these arguments and the disorder observed in the structures of $La_{0.833}Ba_{0.166}MnO_{2.5}$ and $La_{0.8}Ba_{0.2}MnO_{2.5}$, we feel it is appropriate to categorize these phases as being of the disordered intralayer class.

Recent electron diffraction studies are consistent with the presence of disordered intralayer structures for a number of phases that have been structurally characterized with disordered *Imma* models.[4] These often very complex structural arrangements indicate this region of the brownmillerite structure map is itself very complex and that further detailed microstructural investigations will be required to completely unravel this feature of the brownmillerite structural family.

In conclusion, we have prepared and characterized a large number of compositionally related phases with brownmillerite structures. Careful analysis of the structural parameters of these phases has allowed a structure map to be plotted which correlates the appearance of different brownmillerite structural variants with simple crystallographic parameters.

Acknowledgment. We thank the EPSRC for funding this work and E. Suard and R. Smith for assistance collecting the neutron powder diffraction data. We thank Artem Abakumov for the fruitful discussions on the symmetry aspects. The work was supported in part by the IAP VI program of the Belgian government.

Supporting Information Available: Thermogravimetric reoxidation data from all $La_{1-x}A_xMnO_{2.5}$ phases. Fitting statistics from the structural refinement of all brownmillerite models against neutron powder diffraction data collected from all $La_{1-x}A_xMnO_{2.5}$ phases. Observed, calculated and difference plots from the structural refinement against neutron powder diffraction data of all $La_{1-x}A_xMnO_{2.5}$ phases. Complete structural descriptions of $La_{1-x}Ca_xMnO_{2.5}$ (x = 0.3, 0.35, 0.4), $La_{1-x}Sr_xMnO_{2.5}$ (x = 0.2, 0.25, 0.35) and $La_{1-x}Ba_xMnO_{2.5}$ (x = 0.166, 0.25, 0.3) Electron diffraction data collected from $La_{1-x}A_xMnO2.5$ phases. A complete list of brownmillerite phases that contribute to Figure 12 (PDF). This material is available free of charge via the Internet at http://pubs.acs.org.